Journal of Geophysical Research: Solid Earth

RESEARCH ARTICLE
10.1029/2017JB014972

Key Points:
- Earthquake clustering responds differently to hydraulic operations at The Geysers, Coso, and Salton Sea geothermal fields
- The variations of the response are likely related to different local tectonic processes and structures
- Background earthquake rates and types of clusters change between periods of low and high injection-production fluid balance

Supporting Information:
- Supporting Information S1

Correspondence to:
P. Martínez-Garzón,
patricia@gfz-potsdam.de

Citation:
Martínez-Garzón, P., Zaliapin, I., Ben-Zion, Y., Kwiatek, G., & Bohnhoff, M. (2018). Comparative study of earthquake clustering in relation to hydraulic activities at geothermal fields in California. *Journal of Geophysical Research: Solid Earth*, *123*. https://doi.org/10.1029/2017JB014972

Received 9 SEP 2017
Accepted 14 APR 2018
Accepted article online 22 APR 2018

Comparative Study of Earthquake Clustering in Relation to Hydraulic Activities at Geothermal Fields in California

Patricia Martínez-Garzón[1], Ilya Zaliapin[2], Yehuda Ben-Zion[3], Grzegorz Kwiatek[1,4], and Marco Bohnhoff[1,4]

[1]Helmholtz Centre Potsdam, GFZ German Research Centre for Geosciences, Potsdam, Germany, [2]Department of Mathematics and Statistics, University of Nevada, Reno, Reno, NV, USA, [3]Department of Earth Sciences, University of Southern California, Los Angeles, CA, USA, [4]Institute of Geological Sciences, Free University of Berlin, Berlin, Germany

Abstract Earthquake clustering properties are investigated in relation to fluid balance $H(t)$ (the difference of fluid injection and production rates) using about nine years of data from The Geysers (both the entire field and a local subset), Coso, and Salton Sea geothermal fields in California. Individual earthquake clusters are identified and classified using the nearest-neighbor approach of Zaliapin and Ben-Zion (2013a, https://doi.org/10.1785/0120150211, 2013b, https://doi.org/10.1093/gji/ggw300). These are used to calculate nine complementary cluster statistics as time series with a step of about one month. Three alternative techniques (moving window correlation, analysis of variance, and regression) are employed to assess the relations between (possibly nonstationary) time series of cluster statistics and $H(t)$. A total of 108 pairwise relations between cluster statistics and $H(t)$ are analyzed to clarify effects of fluid activities on seismicity in different places. The seismic clustering response to the fluid balance differs among the examined fields. The Geysers and Salton Sea areas display the highest and lowest clustering responses, respectively. The proportion of clusters consisting of a single event with no offspring (singles) is correlated significantly with $H(t)$ at all examined data sets, with a lower proportion of singles during periods of high fluid balance. This may reflect increased susceptibility to earthquake triggering in time intervals with high injection rates. The background seismicity rates significantly increase with $H(t)$ at the Geysers and Coso, while an opposite relation holds at the Salton Sea. This could be related to the high structural and tectonic complexity at the Salton Sea compared to the other two geothermal fields.

1. Introduction

Spatio-temporal clustering of seismicity is a key feature of earthquake phenomenology, although the relative abundance and internal properties of earthquake clusters vary in space and time (e.g., Ben-Zion, 2008; Utsu, 2002; Zaliapin & Ben-Zion, 2016a). Analytical and simulation results in a viscoelastic damage rheology framework suggest that earthquake sequences are controlled by the effective viscosity of a deforming medium and hence should be affected by heat flow, fluid content, and other relevant conditions (Ben-Zion & Lyakhovsky, 2006). Brittle regions with high viscosity (associated with low heat flow and fluid content) are expected to have generally classical (burst-like) aftershock sequences, while partially ductile regions with relatively low viscosity (high heat flow and/or fluid content) are expected to have swarm-like sequences (Zaliapin & Ben-Zion, 2013a). Classification of and discrimination between different earthquake sequences in real data only holds in a statistical sense, due to structural, rheological, and stress heterogeneities along with an interplay of multiple competing mechanisms that drive seismicity. Moreover, a proper statistical analysis should be robust to high variability of space-time earthquake intensities (e.g., nonhomogeneous processes due to transient loadings and induced seismicity) and various errors of earthquake catalogs. The combination of these problems has slowed the development of tools for space-varying characterization of earthquake clusters in relation to local properties of the lithosphere.

Motivated by these challenges, Zaliapin and Ben-Zion (2013a, 2013b) systematically examined properties of earthquake clusters in Southern California with a novel nearest-neighbor approach (see section 3.1). This method allows to robustly identify and analyze seismicity clusters covering a broad range of sizes, energies, and spatio-temporal extents in the presence of varying levels of completeness and uncertainties. Their results highlight the existence of three different basic types of clusters: *burst-like* clusters (reminiscent of classical

aftershock sequences) characterized by a prominently large mainshock, abundance of first-generation offspring, and a small number of foreshocks; *swarm-like* clusters composed of events with comparable magnitudes, each of which has a small number of first-generation offspring, and *singles* that consist of clusters with no offspring. The *burst-* and *swarm-like* clusters in Southern California are dominant in regions with relatively low and high heat flow, respectively, while the *singles* exist everywhere. Zaliapin and Ben-Zion (2016a) confirmed the existence of the three dominant cluster types and their relation to the heat flow (the principal parameter responsible for effective viscosity) on a global scale, in a catalog with higher minimal magnitude and lower location quality than those used in Southern California. These results are consistent with findings of other studies in various regions using alternative techniques (e.g., Enescu et al., 2009; McGuire et al., 2005; Utsu et al., 1995; Vidale et al., 2006; Yang & Ben-Zion, 2009).

The recent boom in shale-gas production and related reservoir activities such as waste-water disposal and geothermal energy production has substantially raised the anthropogenic seismic hazard in the central and eastern United States (e.g., Petersen et al., 2016). Several studies detected differences between properties of seismicity in regular tectonic regions and areas with oil/gas/geothermal explorations. Llenos and Michael (2013) analyzed temporal changes in earthquake rates in Oklahoma and central Arkansas with Epidemic Type Aftershock Sequence (ETAS) modeling (Ogata, 1988). They found that changes in both background seismicity and aftershock productivity are needed to explain the seismicity increase after beginning of fluid injection. They also suggested that regions experiencing significant pore pressure increase should have higher aftershock productivity. Similar results were obtained for the Salton Sea and Brawley geothermal fields (Llenos & Michael, 2016). Comparing the nearest-neighbor interevent times and distances between seismicity in the Coso geothermal field and the surrounding tectonic region, Schoenball et al. (2015) found that the Coso geothermal seismicity display higher background rates and higher rate of earthquake pairs (earthquakes that occur at large times and short distances from their nearest neighbors). Zaliapin and Ben-Zion (2016b) performed a comparative nearest-neighbor analysis of clustering in five regions dominated by tectonic or human-induced earthquakes. They showed that induced seismicity is characterized by (1) higher rate of background events (both absolute and relative to the total rate), (2) faster temporal offspring decay, (3) higher rate of repeaters, (4) larger proportion of small clusters, and (5) larger spatial separation between parent and offspring, compared to regular tectonic activity. These differences have been shown also to discriminate seismicity within the Coso and Salton Sea geothermal fields in California before and after the expansion of geothermal production during the 1980s.

Clarifying further properties of induced seismicity in geothermal environments can contribute to a deeper understanding of seismicity in regions with high fluid content. Geothermal regions tend to be densely monitored with local semipermanent seismic networks, and the corresponding seismicity catalogs tend to cover longer time periods. Long-term changes in background seismicity rates at the three largest geothermal fields in California—The Geysers, Salton Sea, and Coso—have been analyzed with various techniques. Higher background rates were found at The Geysers during time periods of large fluid injection (Johnson et al., 2016; Trugman et al., 2016), while no significant changes in background rate have been reported at Coso (Trugman et al., 2016). At Salton Sea, findings from different studies are not fully consistent (Brodsky & Lajoie, 2013; Llenos & Michael, 2016; Trugman et al., 2016), and additional research is needed to decipher the dynamics of seismicity. In the present study we attempt to clarify how and to what extent earthquake clustering is affected by fluid injection and production. This is addressed by examining consistently four data sets with the cluster detection and classification techniques of Zaliapin and Ben-Zion (2013a, 2013b), and comparing the results with observed time series of injection-production volumes. The rest of the paper is organized as follows. Section 2 describes the examined earthquake catalogs. Section 3 outlines the cluster identification technique and introduces correlation analyses that provide the main contribution of the work. The results and their implications are presented and discussed in sections 4 and 5. The final section 6 summarizes the conclusions.

2. Data and Catalog Processing

We examine the seismicity within The Geysers (Figures 1a and 1b), Coso (Figure 1c), and Salton Sea (Figure 1d) geothermal fields using the double-difference relocated catalogs of northern California (Waldhauser & Schaff, 2008) and southern California (Hauksson & Shearer, 2005; Hauksson et al., 2012). Specific parameters and details

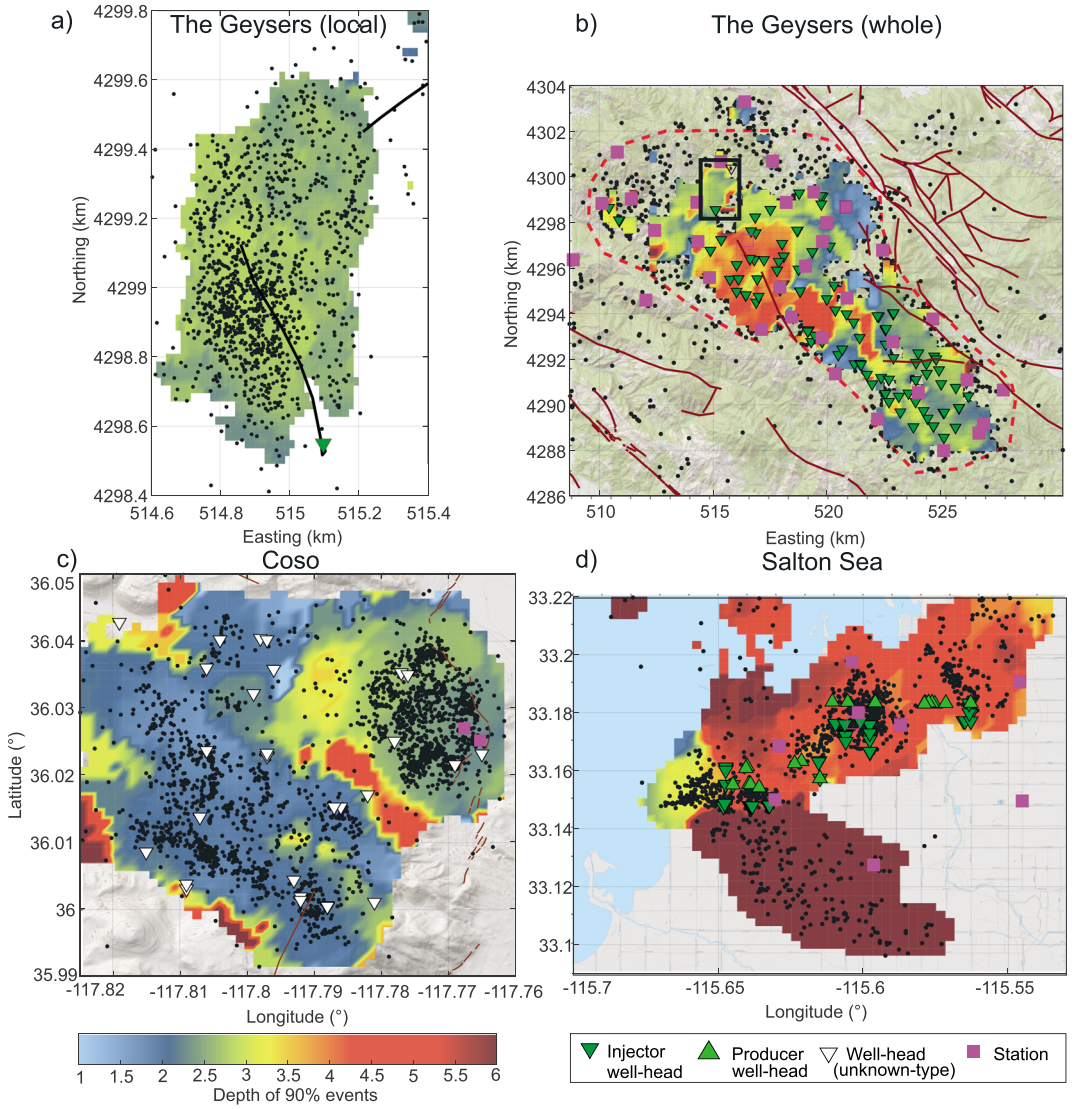

Figure 1. Spatial distribution of the selected seismicity from the four analyzed data sets (black dots) with the map in the background reflecting the depth at which 90% of the seismicity occurs (calculated as the value from the seismicity within a radius between 0.5 and 1 km depending on the field): (a) NW-part of The Geysers (local), (b) The Geysers (whole), (c) Coso, and (d) Salton Sea. The dark green downward triangles represent the active injection wells during the selected time periods. The bright green upward triangles represent the active producer wells. The white donwards triangles represent wells which have changed from injectors to producers or viceversa within the analyzed time. The magenta squares represent the seismic stations with data available for this study. The brown lines represent the quaternary faults included in the USGS database. In (a), the black lines represent the traces of the two local injection wells. In (b) the black rectangle shows the location of The Geysers (local) data set.

for each catalog are given in Table 1. In each of the three regions, we evaluate the temporal evolution of the magnitude M_c of completeness using the maximum curvature method of Woessner and Wiemer (2005) and the approach of Wiemer and Wyss (2000) that estimates M_c as the 10 percentile of the respective Gutenberg-Richter law fit to the data (Figure S1). The moving windows to calculate M_c are set to 100 events in both approaches. The decrease of the estimated M_c values roughly coincides with the installation or enhancement of local networks in each geothermal field. These time periods with relatively lower M_c and denser local network are selected for detailed analysis (the specific time intervals are described below). The *b*-value is estimated following Wiemer and Wyss (2000). Finally, the fractal dimension *d* is estimated using the box-counting for an ensemble of 3-D hypocenters (Schroeder, 1991). Table 1 lists the estimated parameters for the different data sets.

Table 1
Seismicity Parameters and Catalog Statistics From the Four Employed Data Sets

	The Geysers (local)	The Geysers (whole)	Coso	Salton Sea
Available time period	November 2007 to June 2015	January 1984 to December 2015	January 1981 to December 2016	January 1981 to December 2016
Selected time period	November 2007 to June 2015	January 2007 to December 2015	January 2004 to December 2015	January 2008 to December 2015
N events	1,615	30,302	3,472	6,208
λ (Eq/month)	17.5	280	24	64.5
M range	(1, 3.1)	(1, 4.4)	(0.5, 4.1)	(1, 4.2)
M_c	1	1	0.5	1
b	1.22 + − 0.08	1.02 + − 0.004	0.94 + −0.02	0.91 + −0.04
d	2.11 + −0.22	2.12 + −0.10	2.42 + −0.32	2.08 + −0.30
Catalog reference	(Kwiatek et al., 2015; Martínez-Garzón et al., 2014)	(Waldhauser & Schaff, 2008)	(Hauksson & Shearer, 2005; Hauksson et al., 2012)	(Hauksson & Shearer, 2005; Hauksson et al., 2012)
Avg depth (km)	2.4	2.6	1.9	6.0
Avg hor error (km)	0.02	0.02	0.3	0.5
Avg ver error (km)	0.03	0.05	0.6	1.2

Note. Available time period: total time period available from the original relocated catalogs. *Selected time period*: time period analyzed in this study. *N events*: number of events within the selected time period. Λ represents the seismicity rate (events/month). *M range:* minimum and maximum magnitudes contained in the selected subset. M_c: magnitude of completeness. *b*: *b*-value of the Gutenberg-Richter relation. *d:* fractal dimension from the seismicity distribution. *Avg depth*: average depth of the selected events. *Avg hor error*, *avg ver error*: average horizontal and vertical errors from the relocated hypocenter catalogs, respectively.

2.1. The Geysers Geothermal Field, Northern California

The Geysers is the largest geothermal field in California by the steam volume produced. Geothermal operations started around 1960, and water has been injected since the beginning of field operations with the primary purpose of maintaining the reservoir pressure. The earthquake intensity has been shown to correlate well with the injection rates (Eberhart-Phillips & Oppenheimer, 1984; Johnson et al., 2016; Kwiatek et al., 2015; Martínez-Garzón et al., 2013; Trugman et al., 2016), and it is commonly accepted that the local seismicity is mostly induced by the fluid injection. The produced amount of steam is larger than that of the injected water, resulting in field depletion and corresponding subsidence (Mossop & Segall, 1997; Vasco et al., 2013). Aggregated monthly injection and production data for the whole field are publicly available and provided by the Department of Conservation State of California (DCSC). While steam production is maintained roughly constant through the year, the injection volumes have seasonal changes with larger volumes injected in winter season.

The magnitude detection threshold of the examined catalog (Waldhauser & Schaff, 2008) displays a substantial decrease after 2007, when a new type of sensors was installed (Geospace GS-11D sensors replaced SM6 sensors) and the addition of more stations in subsequent years. After 2007, the completeness magnitude mostly remains $M_c < 1$ (Figure S1a). We select for analysis 30,302 events between January 2007 and December 2015. Among these, 30,124 events were characterized by duration magnitude M_d, 106 by local magnitude M_L, and 72 by moment magnitude M_W reported. For uniformity of analysis, we assume as in Kwiatek et al. (2015) that $M_W = M_L$, appropriate for relatively small events (Ben-Zion & Zhu, 2002; Edwards et al., 2010), and estimate M_D from M_W as $M_D = (M_W - 0.47)/0.99$ (Edwards & Douglas, 2013). The resulting event magnitudes are in the range (1.0, 4.4) with the estimated *b*-value $b = 1.02 \pm 0.004$ (Figure S2), in agreement with previous studies (e.g., Convertito et al., 2012).

In addition, we separately analyze the seismicity from an isolated portion (2 km × 2 km) at NW Geysers, where the seismicity is clearly modulated by water injection into two nearby wells, Prati-9 and Prati-29 (Figure 1a). Daily hydraulic data for these two wells are available. Most of the seismicity occurs around the open-hole section of Prati-9 well, but the spatial extent of the seismicity cloud fluctuates according to the injection in both wells (Kwiatek et al., 2015). We employ a subset of 1,615 seismic events from a previously relocated catalog between November 2007 (coinciding with beginning of injection in Prati-9) and June 2015, after removing scattered events in the vicinity of the shallower Prati-29 well. This catalog corresponds to $M_c = 1$ and $b = 1.22 \pm 0.08$ (Kwiatek et al., 2015; Martínez-Garzón et al., 2014; Martínez-Garzón, Kwiatek, et al., 2016). The *b*-value is larger than in the Salton Sea and Coso. This could be related to slight potential

underestimation of M_c at Salton Sea and Coso, or genuine b-value variations reflecting different stress levels and/or different relative proportion of tectonic seismicity.

2.2. Coso Geothermal Field, Eastern California

At Coso, exploration activities started in early 1970s; public production and injection data began in 1987 and the production reached its maximum in 1990 (*DCSC*). Since then, both monthly aggregated injection and production rates have experienced a slow and steady decline, with production rates being approximately two times higher than injection rates. Similar to The Geysers, the injection volumes have seasonal changes, with larger volumes injected in winter time.

Coso is located in a tectonically active area with natural seismicity and several local faults (e.g., Hauksson & Unruh, 2007). The majority of earthquakes are located in the upper 4 km layer (Kaven et al., 2014; Trugman et al., 2016; Figure 1c). The M_c in the relocated catalog (Hauksson et al., 2012; Hauksson & Shearer, 2005) varies in time due to changes in the seismic network (Figure S1b). We select a period between 2004 and 2015 when the estimated M_c from the maximum curvature method mostly remains about 0.5, in good agreement with previous estimations (Hutton et al., 2010; Schoenball et al., 2015). However, this method may slightly underestimate M_c. In total, 3,472 seismic events with local magnitude in the range (0.5, 4.1) are examined. The b-value is estimated as $b = 0.94 \pm 0.02$ (Figure S2), in agreement with previous studies (e.g., Schoenball et al., 2015).

2.3. Salton Sea Geothermal Field, Southern California

Geothermal operations at Salton Sea started in 1982 with a remarkable increase in injection and production volumes in the late 1980s (DCSC). As in the other fields, fluid-production surpasses the injected volumes resulting in significant reservoir depletion and subsidence (Barbour et al., 2016). In contrast to the other fields, no seasonal variations in the injection and production volumes can be easily identified. The Salton Sea geothermal field is located in a tectonically active region characterized by high heat flow and the occurrence of seismic swarms that include dozens of events of similar magnitude within short time periods (Chen & Shearer, 2011). Most of the seismicity is located between 4 and 6 km depth, below the overall reservoir depth of ~2 km (Figure 1d). Monthly injection and production data aggregated for the whole field are available (DCSC). The correlations between hydraulic operations and seismicity rates reported in different studies are not completely consistent. Brodsky and Lajoie (2013) and Llenos and Michael (2016) reported on correlation between background seismicity rates and fluid balance, while Trugman et al. (2016) did not find a clear long-term trend.

We select earthquakes with $M_c \geq 1$ from the Southern California relocated catalog (Hauksson et al., 2012; Hauksson & Shearer, 2005) during 2008–2015, when eight shallow borehole stations were deployed within the field (Figure S1c). During this time period, 6,208 seismic events with M_L within the range (1.0, 4.2) are selected. The estimated b-value is $b = 0.95 \pm 0.03$ (Figure S2), in agreement with other studies (e.g., Trugman et al., 2016).

3. Methodology

In each of the four examined data sets, we identify clusters of seismicity and analyze time-dependent correlations between selected cluster statistics and the hydraulic parameters of geothermal operations. Below we describe the cluster identification methodology, define examined cluster statistics, and introduce the correlation procedure.

3.1. Identification of Earthquake Clusters

The earthquake clusters are identified according to their space-time-magnitude nearest-neighbor proximity (Zaliapin et al., 2008; Zaliapin & Ben-Zion, 2013a, 2013b). The proximity η_{ij} of event j to an earlier event i in the space-time-magnitude domain is defined as (Baiesi & Paczuski, 2004)

$$\eta_{ij} = \begin{cases} t_{ij}\left(r_{ij}\right)^d 10^{-bm_i}, & t_{ij} > 0, \\ \infty, & t_{ij} \leq 0, \end{cases} \tag{1}$$

where $t_{ij} = t_j - t_i$ (in seconds) and r_{ij} (in meters) are the temporal and spatial distances between the earthquakes i and j, respectively; d is the fractal dimension of the hypocenter distribution; b is the b-value of the

Gutenberg-Richter relation; and m_i is the magnitude of the (earlier) event i. The scalar proximity η_{ij} between events can be expressed as the product of its temporal and spatial components normalized by the magnitude of the earlier event i:

$$\eta_{ij} = T_{ij} \cdot R_{ij} \tag{2}$$

$$T_{ij} = t_{ij} 10^{-qbm_i}, R_{ij} = \left(r_{ij}\right)^d 10^{-(1-q)bm_i}, 0 < q < 1. \tag{3}$$

We fix $q = 0.5$, which provides equal weights to the temporal and spatial distances. The b-value and fractal dimension $2 < d < 3$ (describing the seismicity cloud as a structure that cannot fit to a 2-D plane, yet does not fill the entire 3-D spatial volume) are estimated for every region; they are listed in Table 1 and discussed in section 2. In this study, we calculate r_{ij} as the 3-D space distance between events. However, using epicentral locations (with $1 < d < 2$, which describes the seismicity cloud as a structure between a line and a plane) produces similar results. This indicates that the clusters of earthquakes are prominent enough to be similarly identified in the 3-D space of hypocenters and 2-D space of epicentral projections. This robustness provides additional support to our overall conclusions, especially since the event depths have larger errors than the epicentral locations.

For every event j we identify its nearest-neighbor (*parent*) $i = \underset{k}{\operatorname{argmin}}\ \eta_{kj}$ that corresponds to the shortest proximity of equation (1): $\eta_j = \min_i \eta_{ij}$. As illustrated in Figure 2, the distribution of the nearest-neighbor proximities η_j in observed seismicity catalogs is generally bimodal (e.g., Gu et al., 2013; Kossobokov & Nekrasova, 2017; Schoenball et al., 2015; Zaliapin et al., 2008; Zaliapin & Ben-Zion, 2013a, 2016a, 2016b). The long-proximity mode (representing larger rescaled times and/or distances) roughly corresponds to background events, while the short-proximity mode is associated with clustered earthquakes (i.e., foreshocks and aftershocks); we refer to Zaliapin and Ben-Zion (2013a, 2016a) for detailed discussion and illustrations. To separate the two modes of seismicity, we fit a Gaussian mixture model with two modes to the logarithmic proximities $\log_{10} \eta_j$ (Zaliapin & Ben-Zion, 2016a) and select the midpoint between the two modes as a threshold that separates *short* and *long* proximities (lines in Figure 2). Individual clusters are formed by earthquakes that are connected by short proximity links. Each earthquake connected to a parent by a long link is considered a background event and starts a new cluster. The largest event in each cluster is called *mainshock*; all events within the cluster and prior to/after the mainshock are called *foreshock/aftershocks* (see Figure 6 of Zaliapin & Ben-Zion, 2013a). We use the name *offspring* to refer collectively to all events in a cluster following the first one. A *single* is a cluster that consists of a mainshock with no offspring, while the multiple-event clusters are called *families*.

Induced seismicity is conventionally assumed to have time-dependent rates and is approximated by a nonhomogenous Poisson point processes (e.g., Langenbruch et al., 2011). The used clustering methodology is fairly robust with respect to varying background rates, as the rescaled proximities in the cluster mode are typically orders of magnitude smaller than those in the background mode. Accordingly, changes in earthquake proximity caused by varying background rate are not expected to affect cluster identification. A direct verification of this is provided in section 4.2.

3.2. Examined Cluster and Hydraulic Properties

We consider the following cluster statistics, each of which is defined as a time series within a selected examined region. For every examined time series, the value computed in a particular moving window is attributed to the time t that is the median of the times included in the window. The analyzed properties are the following:

1. *Background* $B(t)$, *single* $S(t)$, and *family* $F(t)$ rates, defined as daily counts of first events in all clusters (equivalently, the daily count of clusters), singles (mainshock with no offspring) and families (mainshocks with offspring), respectively, averaged in a moving window of one month. According to these definitions, $B(t) = S(t) + F(t)$.
2. *Median* $\mu(t)$ of the values of the nearest-neighbor proximity η_j between the background events and their parents, averaged within a moving *event* window. The employed moving window sizes are 30, 400, 70, and 90 events for The Geysers (local and whole), Coso, and Salton Sea, respectively. The window step is half of the corresponding window size. The selected windows contain 1–2% of the total seismicity from

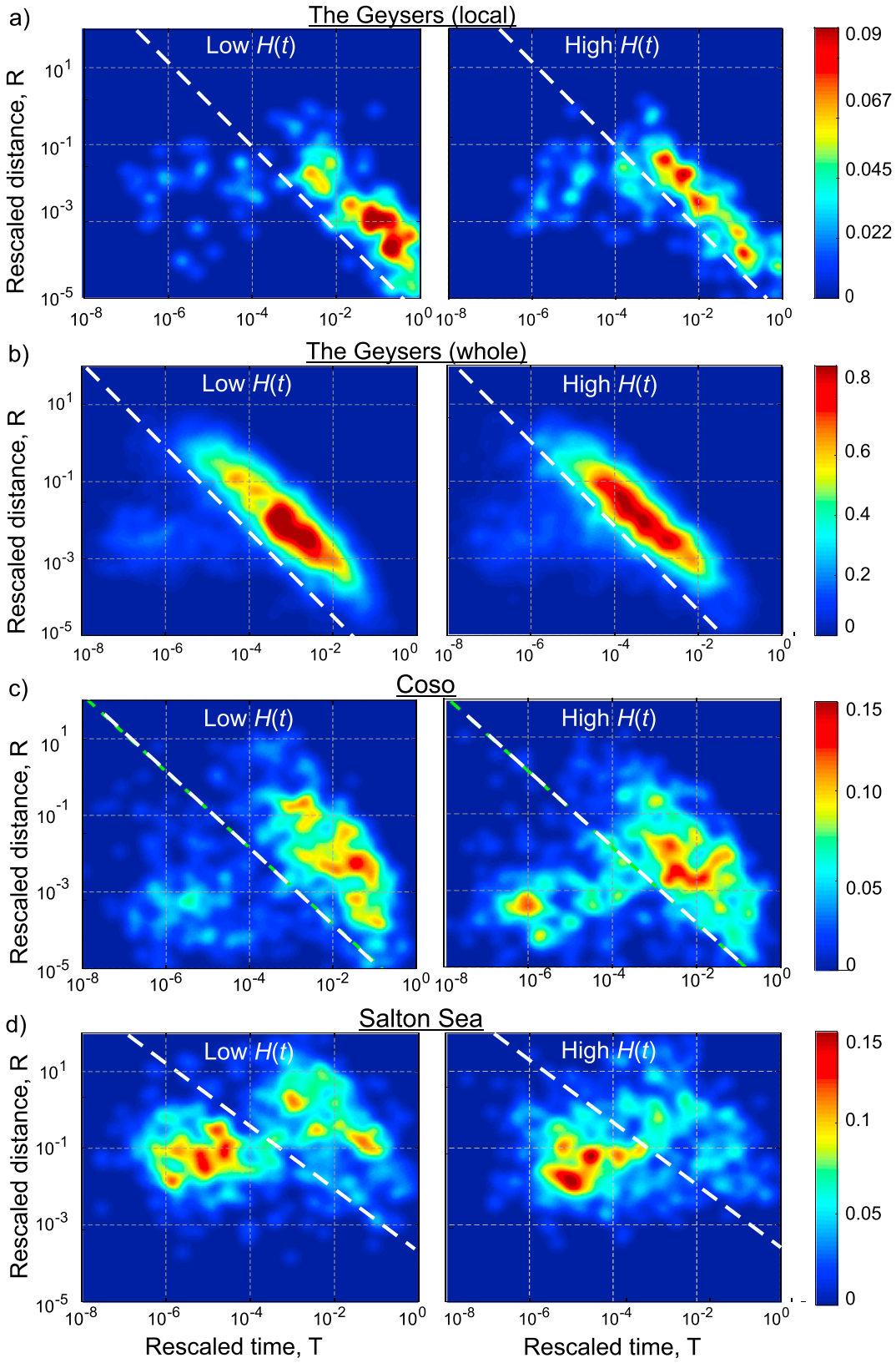

Figure 2. Distribution of rescaled times and distances for the four analyzed data sets. The seismicity contained in the left and right figures represents the 10% of seismicity closer to local minima and maxima of fluid injection balance, respectively. The color bars represent the distribution of the density of event pairs. (a) The Geysers (local), (b) The Geysers (whole), (c) Coso, and (d) Salton Sea.

the corresponding data set, and they ensure sufficient resolution with respect to the hydraulic time series. Variations of the results in response to changing the window sizes to within ±10% are discussed in Text S1.

3. *Rescaled times T*(*t*) and *distances R*(*t*) to parents, averaged within the moving event windows specified in item (2).
4. *Ratio Z*(*t*) of the number of *families* (mainshocks with offspring) to the number of *singles* in a moving time window specified in item (2).
5. *Proportion A*(*t*) of the number of aftershocks to the total number of offspring in a moving window specified in item (2).
6. *Average number N*(*t*) of offspring within the families in a moving event window. Since only a fraction of events have offspring, this analysis uses reduced moving window sizes, three times smaller than those listed in item (2) to maintain comparable temporal resolution with respect to the hydraulic parameters.

The analyzed hydraulic parameter is the reservoir fluid balance $H(t)$ defined as the difference of injection and production rates. This parameter describes the evolving fluid content and provides a better correlation with the examined cluster statistics than either the injection or production data alone. The time series $H(t)$ is filtered to suppress high-frequency fluctuations and focus on robust trends. For The Geysers (local) subset where daily hydraulic data are available, we apply a first-order low-pass Butterworth filter with a normalized cutoff frequency of 0.04π rad/sample. The aggregated monthly hydraulic parameters for The Geysers (whole), Salton Sea, and Coso are only slightly filtered with a first-order low-pass Butterworth filter below the normalized cutoff frequency of 0.95π rad/sample in order to suppress very high frequency signals. The transfer functions of the applied filters are described in Text S2.

In the subsequent sections we introduce three complementary approaches for testing the existence of possible correlations between the earthquake cluster and hydraulic time series.

3.3. Moving Window Correlation Analysis

Let $X(t)$ be one of the cluster statistics time series and $H(t)$ be the fluid balance time series (section 3.2). The time series $X(t)$ and $H(t)$ are interpolated to a common time grid with increment of 30 days, which is a representative interval for the hydraulic time series in the three examined geothermal fields. The Pearson correlation coefficient c_i^{time} is calculated in a moving time window of 6 months (i.e., 6 data points) moving in steps of 1 month (color bars in Figures 4–9, S4, and S7). The choice of this particular window size reflects the existence of seasonal changes in the injection and production time series, which are most prominent at The Geysers geothermal field. The median temporal correlation coefficient $\tilde{c}$ is calculated as a median of the ensemble of correlations coefficients. The correlations are generally robust with respect to different correlation types and window sizes. A detailed discussion on their robustness is provided in Text S1.

The significance of the median correlation $\tilde{c}$ is evaluated in numerical simulations. In general, we seek the probability of observing a correlation stronger than $\tilde{c}$ for two independent time series that are similar to $X(t)$ and $H(t)$. Specifically, we estimate the power spectral density $X(f)$ and $H(f)$ of the examined series using the multitaper approach (Percival & Walden, 1993). Next, we generate n pairs of synthetic time series $\{X'(t)\}_{1\ldots n}$ and $\{H'(t)\}_{1\ldots n}$ by multiplying a random white noise spectrum by the power spectral density spectrum of X (or H) and transfer the resulting spectrum back to the time domain using the inverse Fourier transform (see Figure S3). The resulting simulated series have the same power spectra as the original ones, although their phases are randomly shifted. We calculate the corresponding n median correlation coefficients $c_i^{\text{synthetic}}$ for the n pairs of time series $X'(t)$ and $H'(t)$ using the procedure described above. Finally, the significance (p-value) of the median correlation coefficient $\tilde{c}$ is estimated as the proportion of $c_i^{\text{synthetic}}$ that exceeds $\tilde{c}$. This step takes into account the sign of correlation. If $\tilde{c} > 0$, then $p = \#\left\{c_i^{\text{synthetic}} \geq \tilde{c}\right\}/n$, and if $\tilde{c} < 0$, then $p = \#\left\{c_i^{\text{synthetic}} \leq \tilde{c}\right\}/n$. We use $n = 10{,}000$ and consider the correlation between two time series significant if $p \leq 0.05$; that is, if no more than 50 synthetic pairs out of 10,000 show correlation stronger than that of the observations.

3.4. Regression Analysis

The relation between $X(t)$ and $H(t)$ can also be quantified by the correlation between the entire collection of values in the time series. Specifically, consider the time series $X(t)$ and $H(t)$ interpolated to a 30-day grid,

denoted $\widehat{X}(t)$ and $\widehat{H}(t)$. An iterative linear regression fitting is first applied, which removes up to 10% of the outliers defined via the standard deviation of the linear fitting. Then, the data without outliers are fitted with a standard linear regression. The correlation is measured by (1) the coefficient of determination R^2 and (2) the p-value testing the null hypothesis H_0: The slope of the regression trend between the two variables is equal to zero. The correlation is considered significant if $p \leq 0.05$.

3.5. Analysis of Variance

Finally, we assess the relation between the time series via analysis of variance (ANOVA) that tests the null hypothesis H_0: The means of a selected cluster statistic occurring within time intervals of low and high fluid balance $\widehat{H}$ are the same. Specifically, we divide the values of each cluster time series $\widehat{X}$ into two subgroups corresponding to low ($\widehat{H} <$ median ($\widehat{H}$)) and high ($\widehat{H} >$ median ($\widehat{H}$)) fluid balance. Here we use $\widehat{X}$ and $\widehat{H}$ described in section 3.4 without removing outliers. For every time series $\widehat{X}$, the p-value p^{ANOVA} is computed in a one-way ANOVA test. The null hypothesis H_0 is considered significantly rejected if $p^{\mathrm{ANOVA}} \leq 0.05$.

4. Results

We examine nine earthquake cluster statistics in four regions and use three alternative techniques for establishing relations with the fluid balance $H(t)$. This involves in total examining 108 pairwise relations. The earthquake cluster properties and their correlation with $H(t)$ are different at the three examined geothermal sites. The highest correlation is observed at The Geysers, and the lowest correlation is observed at the Salton Sea. The results are summarized in Table 2. Below we discuss individually each group of cluster statistics.

4.1. Background, Single, and Family Rates

The Geysers (both data sets): the background rates $B(t)$, single rates $S(t)$, and family rates $F(t)$ have significantly higher values during time periods of increased reservoir fluid balance H(t). This is unambiguously confirmed by the three complementary analyses (moving window correlation, regression, and ANOVA; see Figures 3, 4, and S4 and Table 2). In particular, the median correlation coefficient $\widetilde{c}$ is above 0.69 in all six examined cases (three cluster statistics in each of the two areas). The correlations and coefficients of determination are uniformly higher at the local field (Figures 4a and S4a). The observed correlation between $B(t)$ and $H(t)$ is in good agreement with previous studies that used ETAS modeling (Johnson et al., 2016; Trugman et al., 2016).

Coso: significantly higher values of $B(t)$, $S(t)$, and $F(t)$ are observed during time periods of high $H(t)$, although not all analyses provide consistent results. The moving window analysis indicates significant correlation for all three examined cluster statistics, with $\widetilde{c} \geq 0.57$ (Figures 4c and S4a–S4d). However, the regression analysis and ANOVA test indicate a significant change only for the family rates (Table 2 and Figure 3). This implies that while the temporal changes of the cluster statistics correlate significantly with $H(t)$, the largest/smallest values of $B(t)$, $S(t)$, or $F(t)$ do not necessarily coincide with the highest/lowest values of $H(t)$. This also suggests that regression and ANOVA might be less powerful than a moving window analysis in detecting temporal correlations. No correlation between the background rate $B(t)$ and the hydraulic parameters in Coso was previously identified (e.g., Trugman et al., 2016).

Salton Sea: the relations between $B(t)$, $S(t)$, $F(t)$, and $H(t)$ appear more complex than in the other geothermal fields, often reverting their trend with time. A positive but not significant correlation is found between $F(t)$ and $H(t)$ ($\widetilde{c} = 0.21$; Figure S4d). This result is supported by the ANOVA test, indicating a significant positive correlation between $F(t)$ and $H(t)$ (Table 2). The trend between $S(t)$ and $H(t)$ often reverts, and the overall sign of the correlation is negative $\widetilde{c} = -0.26$ (Figure S4d), but the correlation between $S(t)$ and $H(t)$ is only found to be significant by the ANOVA test and regression analysis. Possibly because of these opposite trends between $S(t)$ and $F(t)$, no significant correlation is found between $B(t)$ and $H(t)$ (Figure 4d). These results are in good agreement with the lack of correlation found by long-term fitting of $B(t)$ from ETAS model in Trugman et al. (2016).

The ratio $Z(t)$ between the number of *families* and *singles* differs among the examined fields (Figure 4). At The Geysers and Coso $Z(t) \approx 1/6$, while at Salton Sea $Z(t) \approx 1/3$. However, the temporal evolution of $Z(t)$ is similarly correlated with $H(t)$ at the four data sets according to the significant median correlation coefficient $\widetilde{c} \geq 0.38$, with a higher proportion of families during periods of high $H(t)$ (Figure 5 and Table 2). The data set from The Geysers-local, despite an overall significant and positive correlation, displays a time period with a

Table 2
Results From the Applied Statistical Test and Correlation Techniques to Each Data Set

		The Geysers (local)	The Geysers (whole)	Coso	Salton Sea
$B(t)$ versus $H(t)$	$\tilde{c}$	0.81	0.73	0.64	−0.01
	p-value $\tilde{c}$	0	1.0×10^{-3}	4.0×10^{-4}	0.29
	p^{ANOVA}	1.03×10^{-9}	7.9×10^{-6}	0.07	0.50
	R^2	0.78	0.2	0.02	0.042
	p-value R^2	9.17×10^{-17}	1.3×10^{-5}	0.14	0.067
$F(t)$ versus $H(t)$	$\tilde{c}$	*0.75*	*0.70*	*0.57*	*0.21*
	p-value $\tilde{c}$	0	0.002	0.0021	0.22
	p^{ANOVA}	2.1×10^{-5}	1.2×10^{-11}	0.87	0.0048
	R^2	0.67	0.52	0.04	0.045
	p-value R^2	4.5×10^{-11}	2.1×10^{-5}	0.03	0.057
$S(t)$ versus $H(t)$	$\tilde{c}$	0.79	0.61	0.58	−0.26
	p-value $\tilde{c}$	t)	0.009	3.0×10^{-4}	0.814
	p^{ANOVA}	1.6×10^{-9}	9.3×10^{-4}	0.016	0.044
	R^2	0.72	0.11	5.18×10^{-4}	0.38
	p-value R^2	6.0×10^{-14}	1.3×10^{-4}	0.81	1.26×10^{-9}
$Z(t)$ versus $H(t)$	$\tilde{c}$	0.53	0.50	0.38	0.31
	p-value $\tilde{c}$	0.02	0.03	1.0×10^{-4}	5.0×10^{-4}
	p^{ANOVA}	0.92	7.0×10^{-4}	5.0×10^{-2}	0.15
	R^2	0.002	0.15	0.17	0.25
	p-value R^2	0.75	8.5×10^{-5}	3.9×10^{-6}	8.2×10^{-6}
$1/\mu(t)$ versus $H(t)$	$\tilde{c}$	0.34	0.64	0.17	−0.21
	p-value $\tilde{c}$	0.04	3.0×10^{-3}	0.17	0.83
	p^{ANOVA}	0.12	1.4×10^{-7}	0.04	0.65
	R^2	0.129	0.39	7.91×10^{-4}	0.0042
	p-value R^2	0.0056	1.9×10^{-11}	0.77	0.57
$1/T(t)$ versus $H(t)$	$\tilde{c}$	0.72	0.64	0.45	0.19
	p-value $\tilde{c}$	0	1.6×10^{-3}	0.098	0.18
	p^{ANOVA}	4.3×10^{-4}	0.01	0.006	0.47
	R^2	0.41	0.017	0.02	0.041
	p-value R^2	1.29×10^{-7}	0.21	0.14	0.57
$1/R(t)$ versus $H(t)$	$\tilde{c}$	−0.68	−0.30	−0.20	−0.12
	p-value $\tilde{c}$	3.3×10^{-4}	0.05	0.15	0.72
	p^{ANOVA}	0.002	0.84	0.69	0.89
	R^2	0.3276	5.85×10^{-5}	0.004	0.0059
	p-value R^2	4.9×10^{-6}	0.94	0.49	0.48
$N(t)$ versus $H(t)$	$\tilde{c}$	0.34	0.34	0.39	−0.19
	p-value $\tilde{c}$	0.05	0.05	0.03	0.80
	p^{ANOVA}	0.002	0.02	0.22	0.15
	R^2	0.077	0.04	0.049	0.01
	p-Value R^2	0.048	0.06	0.016	0.29
$A(t)$ versus $H(t)$	$\tilde{c}$	−0.35	−0.09	−0.20	0.31
	p-value $\tilde{c}$	0.015	0.29	0.16	0.0394
	p^{ANOVA}	0.18	0.36	0.38	0.0278
	R^2	0.05	0.09	0.02	0.20
	p-value R^2	0.04	0.003	0.17	3×10^{-5}

Note. The $\tilde{c}$ and p-value $\tilde{c}$ indicate the median temporal correlation coefficient $\tilde{c}$ and the corresponding p-value of the moving window correlation analysis. These coefficients reflect the temporal evolution of the corresponding earthquake clustering property X(t) and the fluid balance $H(t)$. The p^{ANOVA} reflects the significance of the null hypothesis H_0: the means of the distribution of the clustering property $X(t)$ at low and high fluid balance $H(t)$ are statistically equal. The R^2 and p-value R^2 indicate the linear coefficient of determination and the corresponding p-value from the regression analysis. The cell is colored in green if the correlation is considered significant, which is here evaluated if the corresponding p-value is $p \leq 0.05$. Three types of green are used for the three different analyses. $B(t)$, $F(t)$, *and* $S(t)$ represent background, family, and single seismicity rates, respectively. $Z(t)$ indicates the proportion of family to single mainshocks within an event window. $\mu(t)$ indicates the proximity between events. $T(t)$ and $R(t)$ denote the rescaled times and distances, respectively. $N(t)$ and $A(t)$ represent the average number of offspring and the proportion of aftershock to the total amount of offspring within a given event window, respectively.

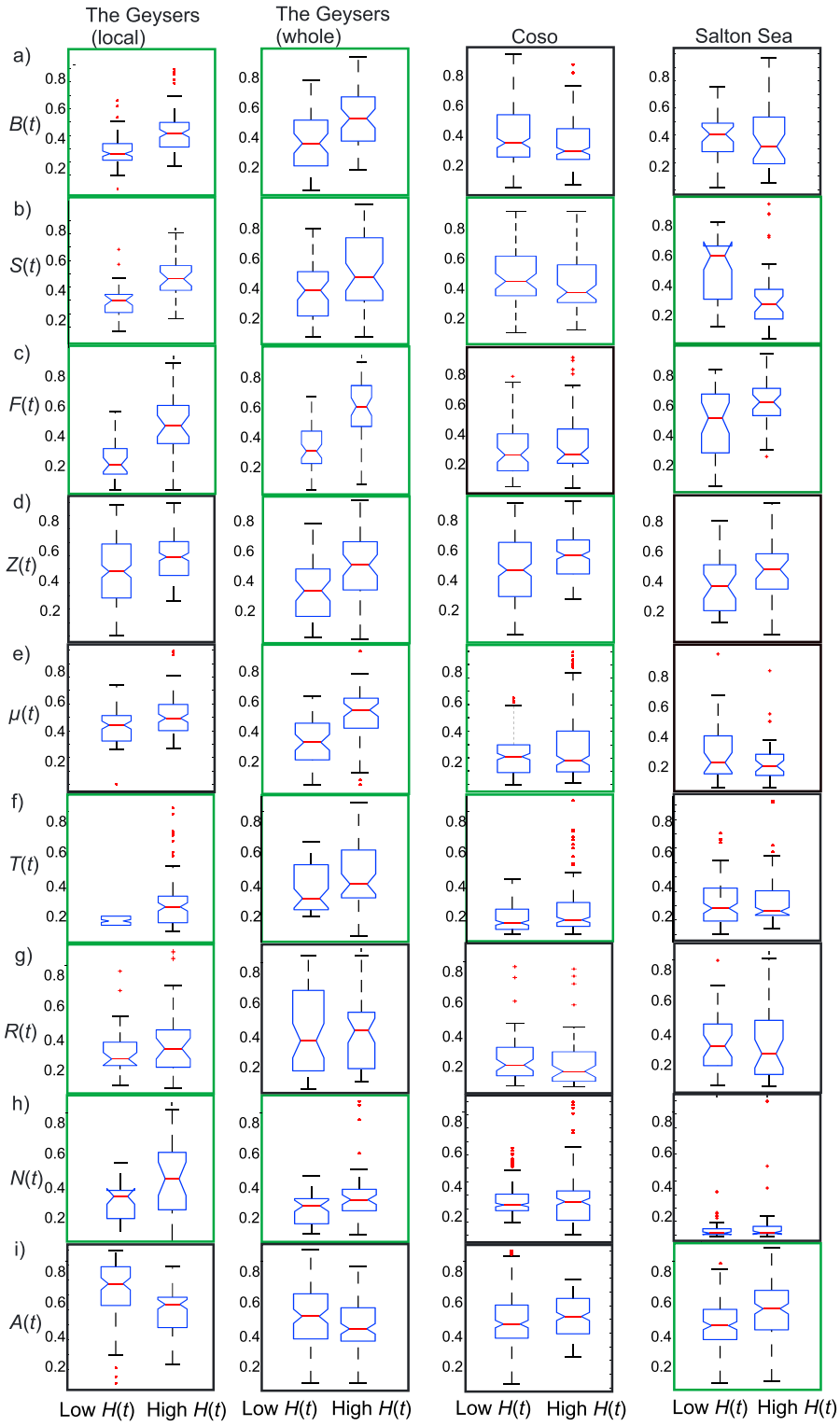

Figure 3. ANOVA analysis results. Multiple statistics that test the null hypothesis H_0: the means from the populations of $X(t)$ during time periods with low and high fluid balance are equal. The results are illustrated using comparative boxplots for low and high fluid balance periods. In each of the boxplots, the red line indicates the median, the blue box extends between the first and third quartiles, and the black dashed lines (whiskers) extend between the minimum and maximum value excluding outliers, which are shown by red points. Normalized boxplots for The Geysers-local, The Geysers-whole, Coso, and Salton Sea are showed in columns from left to right. (a) Background rates $B(t)$, (b) single rates $S(t)$, (c) family rates $F(t)$, (d) proportion of *families* to *singles* $Z(t)$, (e) proximity between events $\mu(t)$, (f) rescaled inter-event time $T(t)$, (g) rescaled inter-event distance $R(t)$, (h) number of offspring $N(t)$, and (i) proportion of aftershocks to total number of offspring $A(t)$. A box is framed in green if the null hypothesis H_0 is rejected (correlation is found) at 5% significance level.

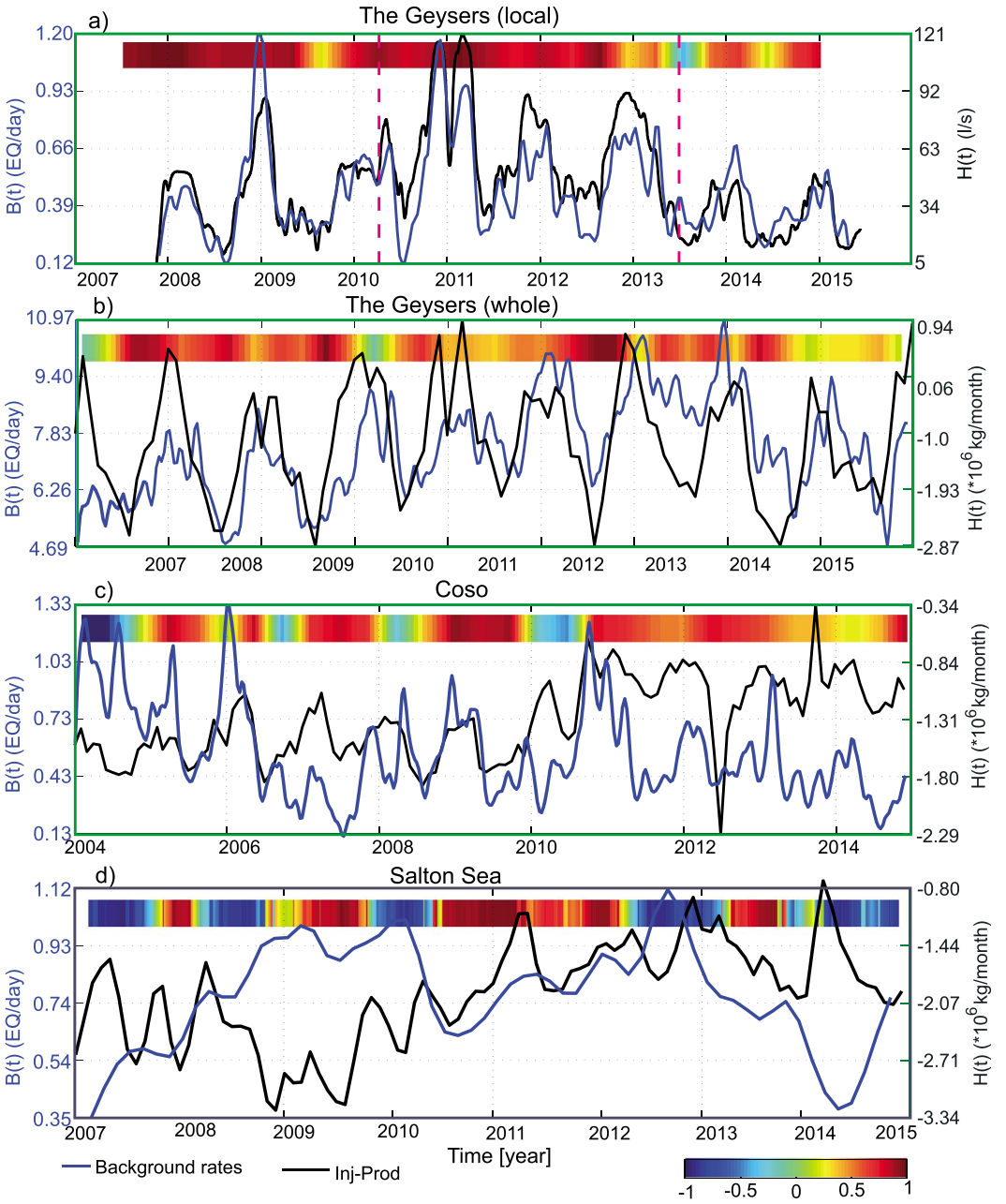

Figure 4. Moving window correlations results. Temporal evolution of the median background seismicity rates ($B(t)$, blue lines) and the fluid balance ($H(t)$, black lines) for (a) The Geysers (local), (b) The Geysers (whole), (c) Coso, and (d) Salton Sea. Note that $H(t)$ at The Geysers (local) represents the injection rates since production is negligible. The dashed magenta lines in (a) mark the start and end of injection in the well Prati-29. The color bars represent the correlation coefficient between the two represented. Each plot is framed in green if the average temporal correlation coefficient is found to be significant ($p < 0.05$).

negative correlation. This period coincides with the shut-in of the nearby well Prati-29 (whose active injection period is indicated with vertical dashed magenta lines in Figures 4a–9a), which affected the local stress field and the seismicity distribution (Kwiatek et al., 2015; Martínez-Garzón, Vavryčuk, et al., 2016). The regression and ANOVA analyses also indicate a significant relation between $Z(t)$ and $H(t)$ at The Geysers (whole field), Coso, and Salton Sea (Table 2 and Figure 5). It is interesting that $Z(t)$ is the only of the examined nine cluster statistics that displays the same trend—increase with $H(t)$—in each of the four data sets considered in this study (Figure 5).

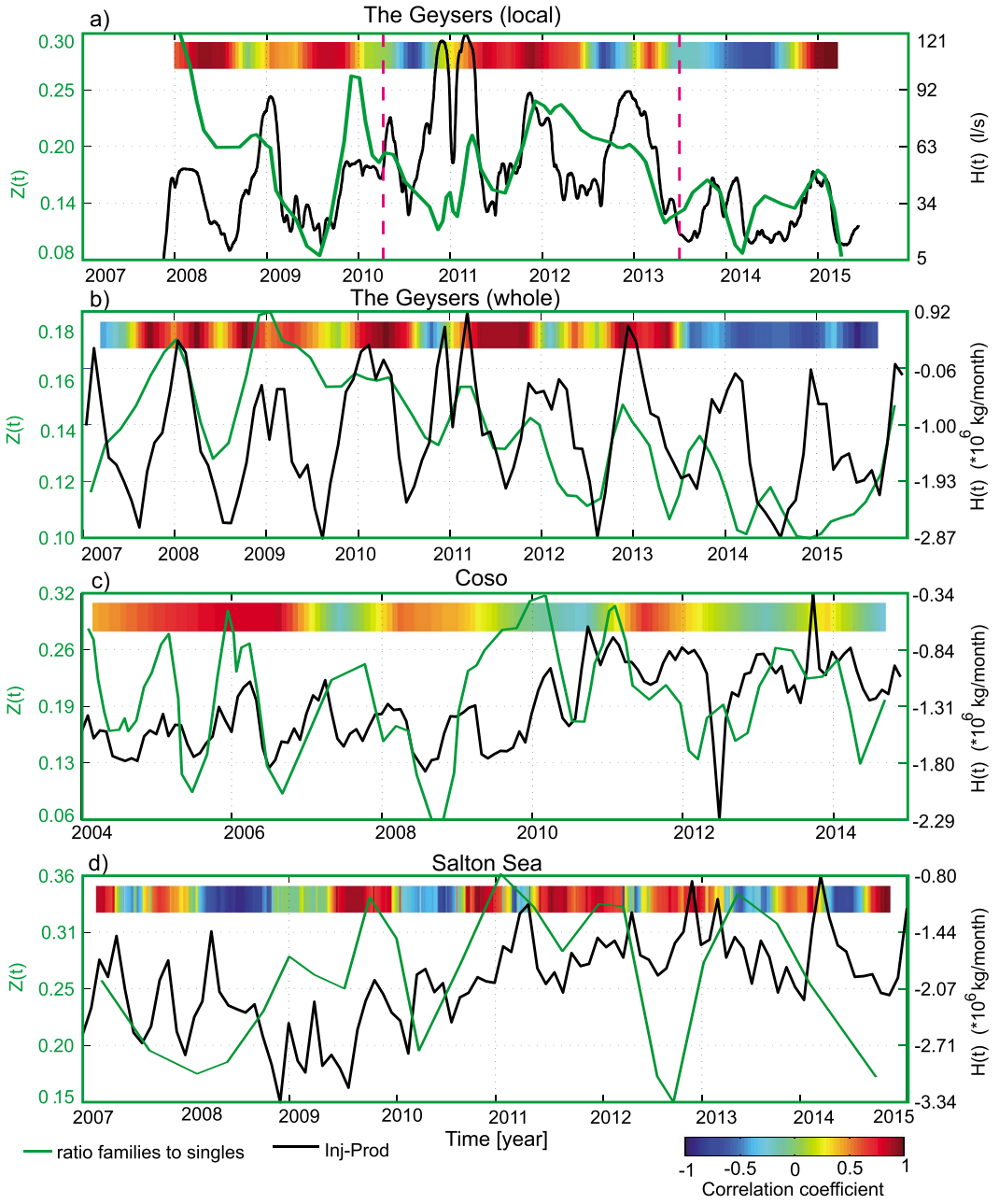

Figure 5. Same as Figure 3 but for the median ratio of family to single main shocks ($Z(t)$, green lines).

We note that our estimated background rates $B(t)$ are higher than those reported in other studies for the same time period using ETAS modeling. These differences may be related to the larger number of singles identified by the nearest-neighbors approach with respect to the ETAS model, as mentioned in Zaliapin and Ben-Zion (2013a).

4.2. Rescaled Interevent Times and Distances and Median Proximity Between Events

The Geysers: a strong positive correlation between $1/T(t)$ and $H(t)$ is clearly confirmed by both moving correlation ($\bar{c} \geq 0.8$) and ANOVA analyses ($p^{ANOVA} \leq 0.01$; Figures 6a and 6b and Table 2). The regression analysis only finds a significant relation for this pair of statistics in The Geysers-local. This could indicate either increased background rates during periods of high $H(t)$, or alternatively, variations in the b-value modulated by the $H(t)$.

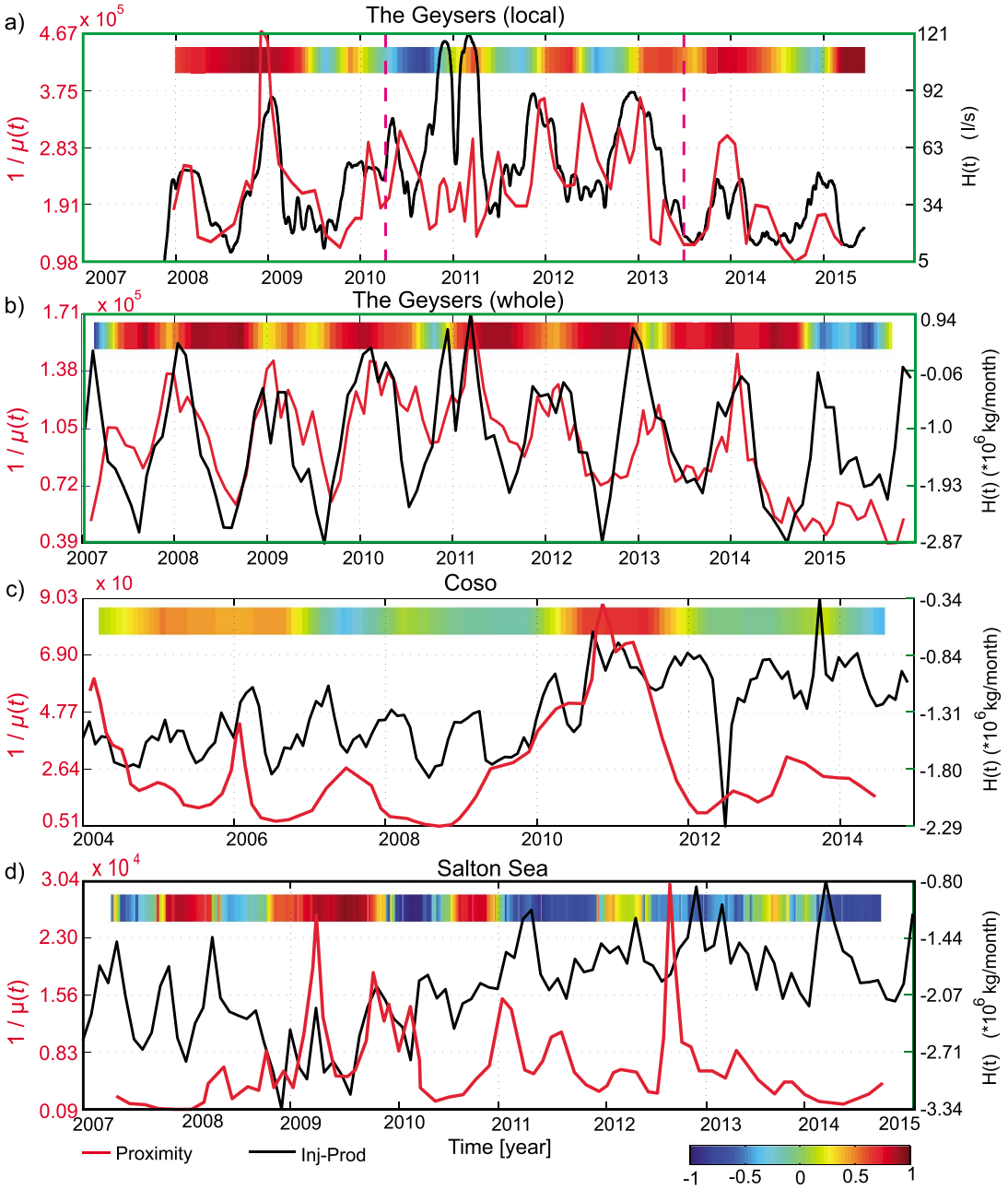

Figure 6. Same as Figure 3 but for the inverse of the proximity between seismic events $\left({}^{1}/_{\mu(t)}\right)$, red lines).

The correlation between $1/R(t)$ and $H(t)$ is significant at The Geysers-local according to all three tests, while at the Geysers-whole it is significant only according to the moving window analysis (Figures S7a and S7b and Table 2). The median correlation coefficients are negative, indicating that during periods of high fluid balance $H(t)$ the seismicity tends to occur at greater rescaled interevent distances, hence possibly activating a greater volume. At the local field, this is in good agreement with previous studies (Kwiatek et al., 2015; Martínez-Garzón et al., 2014). This is shown here to also apply for the whole field, although the correlation is weaker, potentially due to a more complex distribution of injection and production wells (Table 1).

For most of the analyzed years, the temporal evolution of the reciprocal median proximity $1/\mu(t)$ at The Geysers (whole) appears well correlated ($\tilde{c}\approx 0.64$) with the fluid balance $H(t)$. This implies that during periods of higher $H(t)$ the proximity between events is shorter (Table 2 and Figure 6b). Therefore, the observed

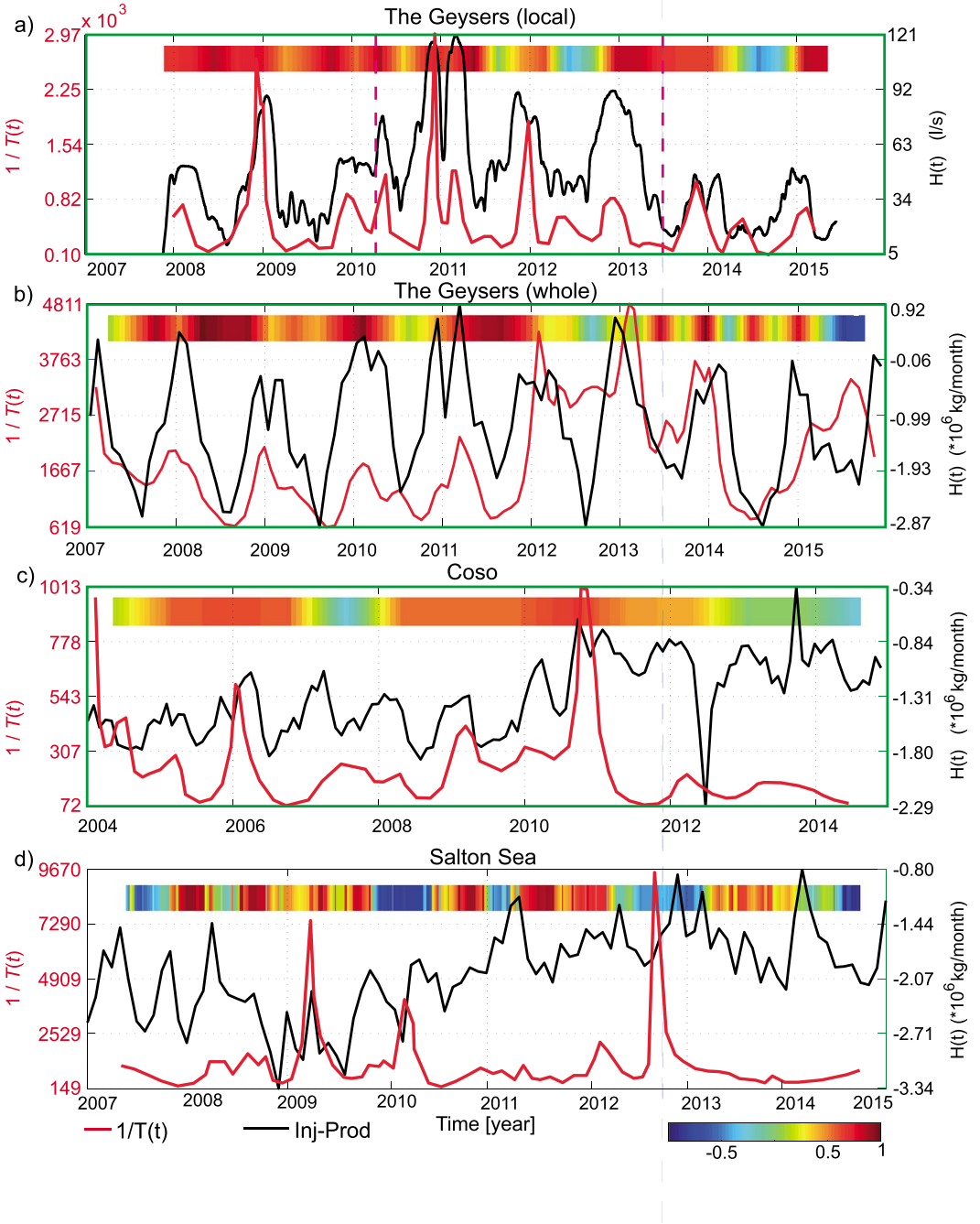

Figure 7. Same as Figure 3 but for the inverse of the inter-event time ($^1/_{T(t)}$).

correlation between $\mu(t)$ and $H(t)$ is largely driven by the strong positive correlation between $1/T(t)$ and $H(t)$, rather than the weaker negative correlation between $1/R(t)$ and $H(t)$ (Table 2). However, at The Geysers (local), both temporal and spatial correlations are strong and opposite in sign, which might result in an overall weaker correlation between $\mu(t)$ and $H(t)$ (Figure 6a and Table 2).

Coso: a weak correlation ($\widetilde{c} = 0.48$) between $1/T(t)$ and $H(t)$ is observed and confirmed by the ANOVA test (Figure 7c and Tables 1 and 2). However, no correlation is found between $H(t)$ and $1/R(t)$ or $\mu(t)$ (Table 2).

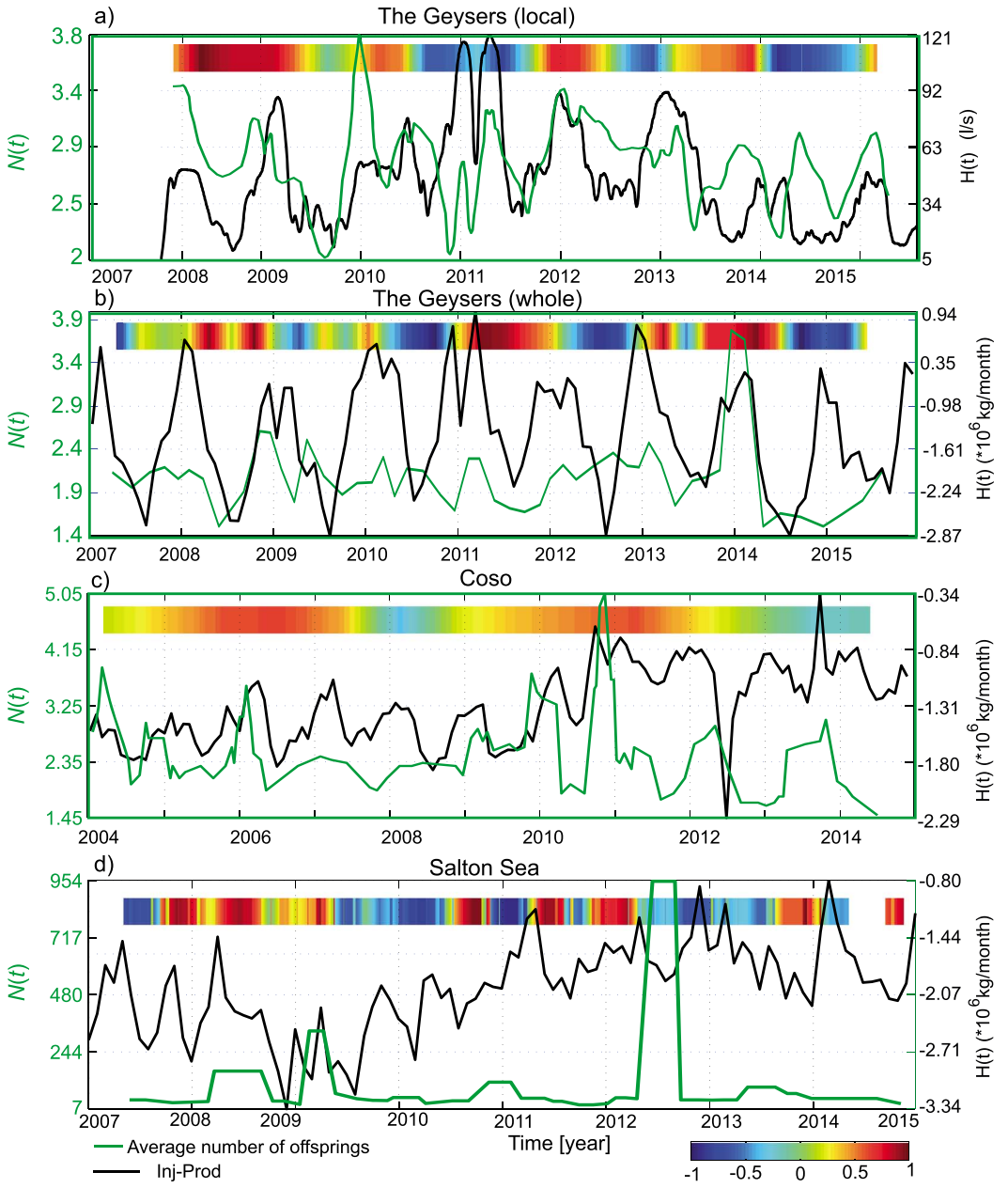

Figure 8. Same as Figure 3 but for the average number of offspring of the family main shocks ($N(t)$, green lines).

Salton Sea: No significant correlations are found between $1/T(t)$, $1/R(t)$, or $1/\mu(t)$ and $H(t)$ at this field by the moving window correlation analysis (Figures 6d, 7d, and S7d and Table 2). Similarly, no significant relations between these parameters are reported by the ANOVA or regression analysis.

We examine further the joint distribution of the rescaled times $T(t)$ and distances $R(t)$ for the events corresponding to about 10% of the seismicity in a temporal vicinity of local fluid balance minima and maxima, respectively. A higher proportion of clustered seismicity is seen at the Salton Sea and Coso during the periods of fluid balance maxima (Figures 2c and 2d), in agreement with the observed high $Z(t)$ during the periods of high $H(t)$. At The Geysers (both data sets), the distributions of (T, R) are dominated by a large population of singles, which prevents making decisive conclusions. The separation line between background and clustered modes (Figure 2) fits well the distributions of seismicity occurring within both low and high injection rates. This supports the claim that changes in background rates do not significantly affect the cluster identification methodology (Zaliapin et al., 2008; Zaliapin & Ben-Zion, 2013a, 2013b).

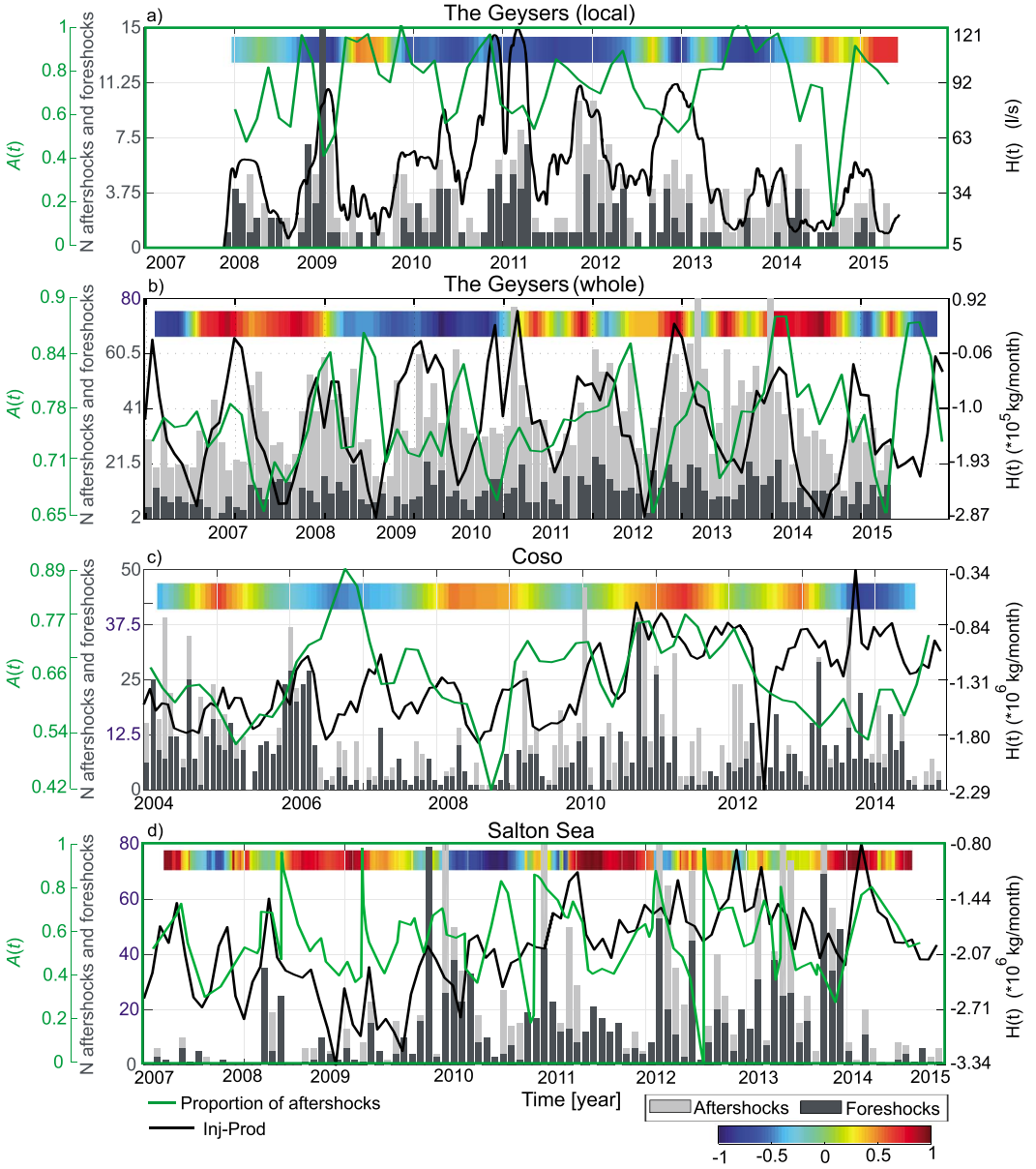

Figure 9. Same as Figure 3 but for the average proportion of aftershocks with respect of total number of offspring within the selected time windows ($A(t)$, green lines). The dark and light grey bars represent the monthly number of foreshocks and aftershocks, respectively.

4.3. Offspring Number and Aftershock Proportion

A weak but significant correlation between the total offspring number $N(t)$ and fluid balance $H(t)$ is established in The Geysers (both data sets) by the moving window analysis and ANOVA test (Figures 8a and 8b and Table 2). The regression analysis gives indecisive results, with the respective p-value being close to 0.05. Taking into account the exponential relation of the total family offspring number to the family mainshock magnitude (Figure S8), the observed correlation can be explained by the mainshock magnitude increase within intervals of high fluid injection. A significant correlation between $N(t)$ and $H(t)$ is also found at Coso geothermal field and supported by the regression analysis (Figure 8c and Table 2). This result is, however, found to be insignificant by the ANOVA test. A possible explanation of this discrepancy in the results of regression analysis versus ANOVA test could be the removal of 10% of outliers in the regression analysis; the outliers may destroy the significant correlation found by regression. No significant correlation between $N(t)$ and $H(t)$ is found at Salton Sea geothermal field (Figure 8d and Table 2).

At The Geysers (local), a weak but significant negative correlation ($\tilde{c} \approx -0.35$) is found between the proportion $A(t)$ of aftershocks with respect to the total number of offspring and $H(t)$, which is confirmed by the regression analysis (Figure 9 and Table 2). This suggests that high fluid balance $H(t)$ stimulates a larger proportion of foreshocks. The ANOVA test does not indicate a significant correlation. The correlations appear insignificant at the whole-field scale according to the moving window correlation and the ANOVA test, but they are reported as significant by the regression analysis.

The absolute numbers of aftershocks and foreshocks are also different between the local and whole areas at The Geysers. At The Geysers (local), the number of aftershocks and foreshocks is comparable, indicating *swarm-like* clustering, during approximately the first three years of stimulation (Figure 9a). In contrast, the monthly number of aftershocks at The Geysers (whole) is remarkably larger than the number of foreshocks (Figure 9b). The difference in the proportion of aftershocks and foreshocks at the two fields can be related to different reservoir fluid volumes and temperatures, which have been previously identified to influence the type of clustering (Zaliapin & Ben-Zion, 2013b). An increased amount of reservoir fluid and higher temperatures are expected for the local data set, with no significant steam production and injection at >250 °C (e.g., Jeanne et al., 2014). In contrast, the total steam production at The Geysers is larger than fluid injection, implying smaller fluid volumes. In addition, substantial reservoir cooling may have occurred since the start of the fluid injection, which happened more than 60 years ago at several locations of the field.

At Coso, the numbers of foreshocks and aftershocks are comparable, which is a characteristic of *swarm-like* clusters (Chen & Shearer, 2011; Zaliapin & Ben-Zion, 2013b, 2016b; Figure 9c and Table 2). No significant relation between $A(t)$ and $H(t)$ is observed, indicating that in this area the relative production of aftershocks and foreshocks is not driven by the geothermal activities (Figure 9c and Tables 1 and 2). At Salton Sea, the numbers of foreshocks and aftershocks are also comparable (Figure 9d). Interestingly, a significant positive correlation between $A(t)$ and $H(t)$ is found by all three approaches (Table 2 and Figure 9d). The observed correlation suggests that the mainshocks occurring during high $H(t)$ tend to have a higher proportion of aftershocks (Figure 9d), which is opposite to what is observed at The Geysers.

5. Discussion

We analyze nine earthquake cluster statistics at The Geysers, Coso, and Salton Sea geothermal fields and compare them to time series of fluid balance (the difference of injection and production) using three complementary correlation tests. The analyses reveal within a diversity of results a number of significant correlations between selected earthquake cluster properties and the fluid balance. Only the family to single ratio is consistent among different fields. The dependence of the findings on the event window size and correlation type is investigated in Text S2 and Tables S1 and S2. In the following, we interpret the most robust correlations obtained.

5.1. Relations Between Cluster Properties and Hydraulic Parameters Across the Fields

The cluster characteristics analyzed above from The Geysers whole and local geothermal fields are highly consistent. This suggests that the local area from the NW part of the field provides a fair representation of the processes that govern earthquake clustering in the whole field. However, the three geothermal fields (The Geysers, Coso, and Salton Sea) display different levels of correlation between cluster properties and fluid balance. The analyzed local NW portion of The Geysers (local) shows the largest amount of significant relations (Table 2), with 23 out of 27 analyses (3 techniques, 9 cluster statistics) and all 9 moving window correlation tests, suggesting significant cluster relation with fluid balance. The results across The Geysers (whole) are generally consistent with those from the local scale, with 21 out of 27 analyses showing significant correlations (Table 2). In particular, 8 out of 9 examined cluster statistics display significant temporal correlations with fluid balance according to the moving window correlation analysis. In Coso, 13 out of 27 analyses indicate significant relation with 6 out of 9 statistics having significant relation of clustering characteristics with fluid balance. The Salton Sea has the lowest response, with only 11 out of 27 analyses suggesting significant relation and 3 out of 9 statistics having significant moving window correlation.

The different responses of cluster properties to the fluid balance within the three different geothermal fields appear to reflect the tectonic and structural complexity of the regions. The Geysers exemplifies the simplest case with no known tectonic seismicity and only few local faults crossing the field. Additionally, the seismicity

there is well modulated by the fluid injection and mostly limited to the reservoir depth (Eberhart-Phillips & Oppenheimer, 1984; Majer & Peterson, 2007). Coso represents an intermediate situation between The Geysers and Salton Sea. It is located in a tectonically active area crossed by several active faults which have experienced *M*5 earthquakes (e.g., Feng & Lees, 1998; Hauksson & Unruh, 2007). At the same time, the majority of the seismicity tends to localize around the open-hole sections of the wells or slightly below (e.g., Kaven et al., 2014) as illustrated in Figure 1c. While not all examined cluster properties correlate significantly with the fluid balance, significant temporal correlations are found between $H(t)$ and the background rates $B(t)$, the family to single ratio $Z(t)$, and interevent times $T(t)$. This suggests that the seismicity within Coso geothermal field might have a larger response to the hydraulic operations than previously described (e.g., Trugman et al., 2016). A possible explanation of the discrepancy with respect to the findings of Trugman et al. (2016) is that we focus on a much shorter time period during which the field was better monitored and M_c is significantly lower.

The Salton Sea is the most complex case study examined here. It is located in an area of high tectonic and structural complexity at the southern end of the San Andreas Fault and is crossed by several orthogonal structures and pull-apart basins. Seismic swarms unrelated to geothermal operations have been reported (Chen & Shearer, 2011), and the seismicity within the field extends several kilometers below the wells (Figure 1d). These factors likely result in complex response of earthquake clustering to fluid balance. The lack of clear correlations at the Salton Sea can also be partially due to the comparatively lower quality of the examined hypocentral catalog. The average vertical error of the events within the field is about 1.2 km (Table 1), which is significantly larger than that for the other examined geothermal fields. Finally, the Salton Sea is also different in the injection-production variations. While The Geysers and Coso have seasonal changes with larger reservoir fluid volume in winter time, the changes in the Salton Sea do not directly correspond to the seasons.

5.2. Background Rate Changes and Mechanisms Driving Seismicity

The background rates $B(t)$ significantly correlate with fluid balance at The Geysers and Coso. At these sites, the time periods of higher $B(t)$ coincide with time periods of the highest $H(t)$, which suggests the highest volumes of fluid in the reservoir. At The Geysers, the production rates are maintained roughly constant in time compared to the strong seasonal fluctuations in the injection rates. Therefore, the increase of $B(t)$ during times of high $H(t)$ possibly indicates that the fluid injection is the main factor driving the seismicity, in agreement with previous observations there (e.g., Eberhart-Phillips & Oppenheimer, 1984; Johnson et al., 2016). At Coso, the net production, the thermal fracturing of the rock due to temperature contrast, and the small local increases in pore pressure due to fluid injection have been previously proposed as mechanisms driving the seismicity (Fialko & Simons, 2000; Schoenball et al., 2015). Our results suggest that the relative pore pressure increase during times of increased reservoir fluid balance (or equivalently, decreased net production) may be particularly acute at this field.

In contrast, the background rates $B(t)$ at Salton Sea do not display significant correlations with the fluid balance $H(t)$. As mentioned, this could possibly be because the seismicity is driven by more complex processes. Previous ETAS-based estimations found a relatively good correlation of the background rates with the net production (Brodsky & Lajoie, 2013; Llenos & Michael, 2016), in agreement with the observed reservoir depletion and field subsidence (Barbour et al., 2016). However, recent studies, also based on ETAS modeling, do not find any significant correlation between these two parameters (Trugman et al., 2016). Our results do not suggest any correlation between $B(t)$ and $H(t)$, possibly due to the opposite trends of the $F(t)$ and $S(t)$ with respect to $H(t)$.

5.3. Swarm-Like Clusters and Increased Proportion of Families in Periods of High $H(t)$

Regions with high heat flow and/or elevated presence of fluids are expected to have relatively low effective viscosity (Ben-Zion & Lyakhovsky, 2006), leading to *swarm-like* clusters with multiple generations of offspring, each of which has a few direct offspring (Zaliapin & Ben-Zion, 2013a, 2016b). This provides a simple explanation for the dominance of *swarm-like* clusters in the three examined geothermal fields (in comparison to tectonic regions, such as the San Jacinto fault zone). Interestingly, the only cluster property that displays uniform and statistically significant temporal correlations with the fluid balance $H(t)$ in all examined data sets is the proportion $Z(t)$ of families with respect to singles. For the four analyzed data sets, $Z(t)$ is observed to be higher during the periods of high $H(t)$. This indicates that background events are more prone, in different structural

and tectonic settings, to have offspring during the periods of high fluid balance. A simple explanation for this tendency is that higher fluid balance $H(t)$ increases overall the stress in the region, leading to higher susceptibly of triggering offspring.

6. Conclusions

Our analyses of correlations between earthquake clustering properties and hydraulic parameters in three different geothermal fields in California using three alternative statistical approaches (moving window correlation, regression analysis, and ANOVA test) can be summarized as follows. Overall, the moving window correlation and regression analyses report the largest and smallest number of significant correlations, respectively. This indicates that the moving window correlation is capable of detecting correlations missed by alternative techniques. At the same time, the moving window approach might be less powerful in rejecting the null hypothesis of absence of correlation, which may facilitate detecting artificial correlations. In general, it is advisable to use a mixture of alternative techniques in correlation analysis of noisy inhomogeneous data. Our results suggest that moving window is the least conservative and the regression analysis is most conservative of the three techniques examined in this work. The following site-specific results are found to be statistically significant:

1. The response of the earthquake cluster properties to hydraulic operations differs from field to field. The earthquake clustering at The Geysers is strongly modulated by temporal changes in the fluid balance. At Coso, the fluid balance plays a weaker role in controlling the earthquake clustering and the Salton Sea area displays the least clear response. These different responses are inversely related to the tectonic complexity of each region—a higher tectonic and structural complexity leads to lower response of clustering to the fluid balance.
2. The proportion of *families* (mainshocks with offspring) with respect to *singles* (mainshocks without offspring) is significantly higher during time periods of high fluid balance in all examined data sets. This is consistent with an overall increased stress in times of high fluid balance that stimulates offspring generation.
3. At The Geysers and Coso geothermal fields, the background seismicity rates are significantly modulated by the fluid balance, suggesting that fluid injection is an important mechanism driving seismicity. In contrast, mixed trends and no significant overall correlation is observed at Salton Sea, likely reflecting a more complex interplay of the combined processes that control seismicity.
4. At The Geysers and Coso geothermal fields, the rescaled interevent times between mainshocks tend to decrease during periods of high fluid balance. This is in good agreement with the reported higher background rates, but it could also be indicative for a slightly lower *b*-value during these times. At the same time, the rescaled interevent distances increase at The Geysers during high fluid balance periods, possibly suggesting that seismicity propagates away from the wells and activate larger volumes.
5. At the Geysers, mainshocks with the largest numbers of offspring occur during periods of high fluid balance. This might be related to the increase of mainshock magnitude during high fluid balance periods, and not only to increase in aftershock productivity.
6. The aftershock/foreshock proportions significantly change with fluid balance at The Geysers and Salton Sea. The direction of this effect differs between the fields—a higher fluid balance is associated with higher proportion of foreshocks at The Geysers but with higher proportion of aftershocks at Salton Sea.
7. The local area at the NW Geysers is representative of the whole field in terms of relations between fluid balance and earthquake clustering.

Acknowledgments
We are grateful to Martin Schoenball, Christopher Johnson an anonymous reviewer, an anonymous Associate Editor, and Editor Martha Savage for their useful comments. P. M. G. acknowledges funding from the Helmholtz Association in the frame of the Helmholtz Postdoc Programme. I. Z. and Y. B. Z. acknowledge support from the Earthquake Hazards Program of the USGS (grants G17AP00086 and G17AP00087) and the National Science Foundation (grants EAR-1723033 and EAR-1722561). GK acknowledges funding from DFG (German Science Foundation), grant KW84/4-1. We thank Egill Hauksson and Felix Waldhauser for sharing their relocated hypocenter seismicity catalogs. The relocated catalog of Southern California is available from http://scedc.caltech.edu/research-tools/altcatalogs.html (last accessed: 2018-04-05). The relocated catalog of Northern California is available at: http://www.ldeo.columbia.edu/~felixw/NCAeqDD/ (last accessed: April 5, 2018). Monthly hydraulic data from The Geysers, Coso, and Salton Sea are available at the website from Department of Conservation State of California. We thank Craig Hartline and Calpine Corporation Ltd. for sharing daily injection data from the wells Prati9 and Prati29.

References

Baiesi, M., & Paczuski, M. (2004). Scale-free networks of earthquakes and aftershocks. *Physical Review E*, *69*(6), 066106. https://doi.org/10.1103/PhysRevE.69.066106

Barbour, A. J., Evans, E. L., Hickman, S. H., & Eneva, M. (2016). Subsidence rates at the southern Salton Sea consistent with reservoir depletion. *Journal of Geophysical Research: Solid Earth*, *121*, 5308–5327. https://doi.org/10.1002/2016JB012903

Ben-Zion, Y. (2008). Collective behavior of earthquakes and faults: Continuum-discrete transitions, progressive evolutionary changes, and different dynamic regimes. *Reviews of Geophysics*, *46*, RG4006. https://doi.org/10.1029/2008RG000260

Ben-Zion, Y., & Lyakhovsky, V. (2006). Analysis of aftershocks in a lithospheric model with seismogenic zone governed by damage rheology. *Geophysical Journal International*, *165*(1), 197–210. https://doi.org/10.1111/j.1365-246X.2006.02878.x

Ben-Zion, Y., & Zhu, L. (2002). Potency-magnitude scaling relations for Southern California earthquakes with $1.0 < M_L < 7.0$. *Geophysical Journal International*, *148*(3), F1–F5. https://doi.org/10.1046/j.1365-246X.2002.01637.x

Brodsky, E. E., & Lajoie, L. J. (2013). Anthropogenic seismicity rates and operational parameters at the Salton Sea Geothermal Field. *Science*, *341*(6145), 543–546. https://doi.org/10.1126/science.1239213

Chen, X., & Shearer, P. M. (2011). Comprehensive analysis of earthquake source spectra and swarms in the Salton Trough, California. *Journal of Geophysical Research*, *116*, B09309. https://doi.org/10.1029/2011JB008263

Convertito, V., Maercklin, N., Sharma, N., & Zollo, A. (2012). From induced seismicity to direct time-dependent seismic hazard. *Bulletin of the Seismological Society of America*, *102*(6), 2563–2573. https://doi.org/10.1785/0120120036

Eberhart-Phillips, D., & Oppenheimer, D. H. (1984). Induced seismicity in The Geysers Geothermal Area, California. *Journal of Geophysical Research*, *89*(B2), 1191–1207. https://doi.org/10.1029/JB089iB02p01191

Edwards, B., Allmann, B., Fah, D., & Clinton, J. (2010). Automatic computation of moment magnitudes for small earthquakes and the scaling of local to moment magnitude. *Geophysical Journal International*, *183*(1), 407–420. https://doi.org/10.1111/j.1365-246X.2010.04743.x

Edwards, B., & Douglas, J. (2013). Magnitude scaling of induced earthquakes. *Geothermics*, *52*, 132–139. https://doi.org/10.1016/j.geothermics.2013.09.012

Enescu, B., Hainzl, S., & Ben-Zion, Y. (2009). Correlations of seismicity patterns in Southern California with surface heat flow data. *Bulletin of the Seismological Society of America*, *99*(6), 3114–3123. https://doi.org/10.1785/0120080038

Feng, Q., & Lees, J. M. (1998). Microseismicity, stress, and fracture in the Coso geothermal field, California. *Tectonophysics*, *289*(1–3), 221–238. https://doi.org/10.1016/S0040-1951(97)00317-X

Fialko, Y., & Simons, M. (2000). Deformation and seismicity in the Coso geothermal area, Inyo County, California: Observations and modeling using satellite radar interferometry. *Journal of Geophysical Research*, *105*(B9), 21,781–21,793. https://doi.org/10.1029/2000JB900169

Gu, C., Schumann, A. Y., Baiesi, M., & Davidsen, J. (2013). Triggering cascades and statistical properties of aftershocks. *Journal of Geophysical Research: Solid Earth*, *118*, 4278–4295. https://doi.org/10.1002/jgrb.50306

Hauksson, E., & Shearer, P. (2005). Southern California hypocenter relocation with waveform cross-correlation, Part 1: Results using the double-difference method. *Bulletin of the Seismological Society of America*, *95*(3), 896–903. https://doi.org/10.1785/0120040167

Hauksson, E., & Unruh, J. (2007). Regional tectonics of the Coso geothermal area along the intracontinental plate boundary in central eastern California: Three-dimensional Vp and Vp/Vs models, spatial-temporal seismicity patterns, and seismogenic deformation. *Journal of Geophysical Research*, *112*, B06309. https://doi.org/10.1029/2006JB004721

Hauksson, E., Yang, W., & Shearer, P. M. (2012). Waveform relocated earthquake catalog for Southern California (1981 to June 2011). *Bulletin of the Seismological Society of America*, *102*(5), 2239–2244. https://doi.org/10.1785/0120120010

Hutton, K., Woessner, J., & Hauksson, E. (2010). Earthquake monitoring in Southern California for seventy-seven years (1932–2008). *Bulletin of the Seismological Society of America*, *100*(2), 423–446. https://doi.org/10.1785/0120090130

Jeanne, P., Rutqvist, J., Hartline, C., Garcia, J., Dobson, P. F., & Walters, M. (2014). Reservoir structure and properties from geomechanical modeling and microseismicity analyses associated with an enhanced geothermal system at The Geysers, California. *Geothermics*, *51*, 460–469. https://doi.org/10.1016/j.geothermics.2014.02.003

Johnson, C. W., Totten, E. J., & Bürgmann, R. (2016). Depth migration of seasonally induced seismicity at The Geysers geothermal field. *Geophysical Research Letters*, *43*, 6196–6204. https://doi.org/10.1002/2016GL069546

Kaven, J. O., Hickman, S., & Davatzes, N. C. (2014). Micro-seismicity and seismic moment release within the Coso Geothermal Field, California. In *Stanford Geothermal Workshop, Proceedings, 39th Wortkshop on Geothermal Reservoir Engineering* (p. 10). Stanford, CA: Stanford University. Retrieved from https://pangea.stanford.edu/ERE/db/GeoConf/papers/SGW/2014/Kaven.pdf

Kossobokov, V. G., & Nekrasova, A. K. (2017). Characterizing aftershock sequences of the recent strong earthquakes in Central Italy. *Pure and Applied Geophysics*, *174*(10), 3713–3723. https://doi.org/10.1007/s00024-017-1624-9

Kwiatek, G., Martínez-Garzón, P., Dresen, G., Bohnhoff, M., Sone, H., & Hartline, C. (2015). Effects of long-term fluid injection on induced seismicity parameters and maximum magnitude in northwestern part of The Geysers geothermal field. *Journal of Geophysical Research: Solid Earth*, *120*, 7085–7101. https://doi.org/10.1002/2015JB012362

Langenbruch, C., Dinske, C., & Shapiro, S. A. (2011). Inter event times of fluid induced earthquakes suggest their Poisson nature. *Geophysical Research Letters*, *38*, L21302. https://doi.org/10.1029/2011GL049474

Llenos, A. L., & Michael, A. J. (2013). Modeling earthquake rate changes in Oklahoma and Arkansas: Possible signatures of induced seismicity. *Bulletin of the Seismological Society of America*, *103*(5), 2850–2861. https://doi.org/10.1785/0120130017

Llenos, A. L., & Michael, A. J. (2016). Characterizing potentially induced earthquake rate changes in the Brawley Seismic Zone, Southern California. *Bulletin of the Seismological Society of America*, *106*(5), 2045–2062. https://doi.org/10.1785/0120150053

Majer, E. L., & Peterson, J. E. (2007). The impact of injection on seismicity at The Geysers, California Geothermal Field. *International Journal of Rock Mechanics and Mining Sciences*, *44*(8), 1079–1090. https://doi.org/10.1016/j.ijrmms.2007.07.023

Martínez-Garzón, P., Bohnhoff, M., Kwiatek, G., & Dresen, G. (2013). Stress tensor changes related to fluid injection at The Geysers geothermal field, California. *Geophysical Research Letters*, *40*(11), 2596–2601. https://doi.org/10.1002/grl.50438

Martínez-Garzón, P., Kwiatek, G., Bohnhoff, M., & Dresen, G. (2016). Impact of fluid injection on fracture reactivation at The Geysers geothermal field. *Journal of Geophysical Research: Solid Earth*, *121*, 7432–7449. https://doi.org/10.1002/2016JB013137

Martínez-Garzón, P., Kwiatek, G., Sone, H., Bohnhoff, M., Dresen, G., & Hartline, C. (2014). Spatiotemporal changes, faulting regimes, and source parameters of induced seismicity: A case study from The Geysers geothermal field. *Journal of Geophysical Research: Solid Earth*, *119*, 8378–8396. https://doi.org/10.1002/2014JB011385

Martínez-Garzón, P., Vavryčuk, V., Kwiatek, G., & Bohnhoff, M. (2016). Sensitivity of stress inversion of focal mechanisms to pore pressure changes. *Geophysical Research Letters*, *43*, 8441–8450. https://doi.org/10.1002/2016GL070145

McGuire, J. J., Boettcher, M. S., & Jordan, T. H. (2005). Foreshock sequences and short-term earthquake predictability on East Pacific Rise transform faults. *Nature*, *434*(7032), 457–461. https://doi.org/10.1038/nature03377

Mossop, A., & Segall, P. (1997). Subsidence at The Geysers Geothermal Field, N. California from a comparison of GPS and leveling surveys. *Geophysical Research Letters*, *24*(14), 1839–1842. https://doi.org/10.1029/97GL51792

Ogata, Y. (1988). Statistical models for earthquake occurrences and residual analysis for point processes. *Journal of the American Statistical Association*, *83*(401), 9–27. https://doi.org/10.1080/01621459.1988.10478560

Percival, D. B., & Walden, A. T. (1993). *Spectral analysis for physical applications: Multitaper and conventional univariate techniques*. Cambridge, UK: Cambridge University Press. https://doi.org/10.1017/CBO9780511622762

Petersen, M. D., Mueller, C. S., Moschetti, M. P., Hoover, S. M., Llenos, A. L., Ellsworth, W. L., et al. (2016). Seismic-hazard forecast for 2016 including induced and natural earthquakes in the central and eastern United States. *Seismological Research Letters*, *87*(6), 1327–1341. https://doi.org/10.1785/0220160072

Schoenball, M., Davatzes, N. C., & Glen, J. M. G. (2015). Differentiating induced and natural seismicity using space-time-magnitude statistics applied to the Coso geothermal field. *Geophysical Research Letters*, *42*, 6221–6228. https://doi.org/10.1002/2015GL064772

Schroeder, M. (1991). *Fractals, chaos, power laws: Minutes from an infinite paradise*. New York: W. H. Freeman.
Trugman, D. T., Shearer, P. M., Borsa, A. A., & Fialko, Y. (2016). A comparison of long-term changes in seismicity at The Geysers, Salton Sea, and Coso geothermal fields. *Journal of Geophysical Research: Solid Earth*, *121*, 225–247. https://doi.org/10.1002/2015JB012510
Utsu, T. (2002). Statistical features of seismology. In *International Handbook of Earthquake and Engineering Seismology* (pp. 719–732). New York: Academic Press. https://doi.org/10.1016/S0074-6142(02)80246-7
Utsu, T., Ogata, Y., & Matsu'ura, R. S. (1995). The centenary of the Omori formula for a decay law of aftershock activity. *Journal of Physics of the Earth*, *43*(1), 1–33. https://doi.org/10.4294/jpe1952.43.1
Vasco, D. W., Rutqvist, J., Ferretti, A., Rucci, A., Bellotti, F., Dobson, P., et al. (2013). Monitoring deformation at the Geysers Geothermal Field, California using C-band and X-band interferometric synthetic aperture radar. *Geophysical Research Letters*, *40*, 2567–2572. https://doi.org/10.1002/grl.50314
Vidale, J. E., Boyle, K. L., & Shearer, P. M. (2006). Crustal earthquake bursts in California and Japan: Their patterns and relation to volcanoes. *Geophysical Research Letters*, *33*, L20313. https://doi.org/10.1029/2006GL027723
Waldhauser, F., & Schaff, D. P. (2008). Large-scale relocation of two decades of Northern California seismicity using cross-correlation and double-difference methods. *Journal of Geophysical Research*, *113*, B08311. https://doi.org/10.1029/2007JB005479
Wiemer, S., & Wyss, M. (2000). Minimum magnitude of completeness in earthquake catalogs: Examples from Alaska, the western United States & Japan. *Bulletin of the Seismological Society of America*, *90*(4), 859–869. https://doi.org/10.1785/0119990114
Woessner, J., & Wiemer, S. (2005). Assessing the quality of earthquake catalogues: Estimating the magnitude of completeness and its uncertainty. *Bulletin of the Seismological Society of America*, *95*(2), 684–698. https://doi.org/10.1785/0120040007
Yang, W., & Ben-Zion, Y. (2009). Observational analysis of correlations between aftershock productivities and regional conditions in the context of a damage rheology model. *Geophysical Journal International*, *177*(2), 481–490. https://doi.org/10.1111/j.1365-246X.2009.04145.x
Zaliapin, I., & Ben-Zion, Y. (2013a). Earthquake clusters in southern California I: Identification and stability. *Journal of Geophysical Research: Solid Earth*, *118*, 2847–2864. https://doi.org/10.1002/jgrb.50179
Zaliapin, I., & Ben-Zion, Y. (2013b). Earthquake clusters in southern California II: Classification and relation to physical properties of the crust. *Journal of Geophysical Research: Solid Earth*, *118*, 2865–2877. https://doi.org/10.1002/jgrb.50178
Zaliapin, I., & Ben-Zion, Y. (2016a). Discriminating characteristics of tectonic and human-induced seismicity. *Bulletin of the Seismological Society of America*, *106*(3), 846–859. https://doi.org/10.1785/0120150211
Zaliapin, I., & Ben-Zion, Y. (2016b). A global classification and characterization of earthquake sclusters. *Geophysical Journal International*, *207*(1), 608–634. https://doi.org/10.1093/gji/ggw300
Zaliapin, I., Gabrielov, A., Keilis-Borok, V., & Wong, H. (2008). Clustering analysis of seismicity and aftershock identification. *Physical Review Letters*, *101*(1), 018501. https://doi.org/10.1103/PhysRevLett.101.018501